

Accepted by *The Astrophysical Journal*, 15 October 2001

HST Imaging in the Chandra Deep Field South: II. WFPC2 Observations of an X-Ray Flux-Limited Sample from the 1 Msec Chandra Catalog¹

Anton M. Koekemoer, Norman A. Grogin, Ethan J. Schreier

Space Telescope Science Institute, 3700 San Martin Drive, Baltimore, MD 21218, USA

R. Giacconi, R. Gilli, L. Kewley, C. Norman, A. Zirm

Department of Physics and Astronomy, Johns Hopkins University, Baltimore, MD 21218, USA

J. Bergeron, P. Rosati

European Southern Observatory, Karl-Schwarzschild-Strasse 2, Garching, D-85748, Germany

G. Hasinger

Astrophysikalisches Institut, An der Sternwarte 16, Potsdam 14482 Germany

P. Tozzi

Osservatorio Astronomico di Trieste, Via G. B. Tiepolo 11, 34131 Trieste Italy

A. Marconi

Osservatorio Astrofisico di Arcetri, Largo E. Fermi 5, 50125 Firenze, Italy

ABSTRACT

We present *HST*/WFPC2 observations of a well-defined sample of 40 X-ray sources with X-ray fluxes above the detection threshold of the full 1 Msec Chandra Deep Field South (CDFS). The sensitivity and spatial resolution of our *HST* observations are sufficient to detect the optical counterparts of 37 of the X-ray sources, yielding information on their morphologies and environments. In this paper we extend the results obtained in our previous study on the 300 ks CDFS X-ray data (Schreier et al. 2001, Paper I). Specifically, we show that the optical

counterparts to the X-ray sources are divided into two distinct populations: 1) an optically faint group with relatively blue colors, similar to the faint blue field galaxy population, and 2) an optically brighter group, including resolved galaxies with average colors significantly redder than the corresponding bright field galaxy population. The brighter objects comprise a wide range of types, including early and late type galaxies, starbursts, and AGN. By contrast, we show that the faint blue X-ray population are most consistent with being predominantly Type 2 AGN of low to moderate luminosity, located at higher redshifts ($z \sim 1 - 2$). This conclusion is supported by luminosity function models of the various classes of objects. Hence, the combination of deep X-ray data with the high spatial resolution of *HST* are for the first time allowing us to probe the faint end of the AGN luminosity function at cosmologically interesting redshifts.

Subject headings: X-rays: galaxies — galaxies: active — galaxies: evolution — galaxies: high-redshift — surveys

1. Introduction

A principal question in astrophysics today involves understanding the formation and evolution of galaxies. Central to this is the connection between large scale structure formation, hierarchical mergers, and the presence of supermassive black holes at the centers of most galaxies (e.g., Magorrian et al. 1998). Addressing these issues requires detailed multi-waveband observations of a variety of galaxy classes, including normal galaxies, starbursts and active galactic nuclei (AGN). Deep X-ray surveys in recent years have provided a wealth of new information on the properties of AGN and starbursts, and their role in galaxy evolution (e.g., Hasinger et al. 1998, 1999; Miyaji et al. 2000). For example, the observed strong evolution of the low end of the AGN luminosity function at high redshifts is likely related to an increased rate of interactions and distorted/irregular morphologies in the early universe (Lilly et al. 1998; Abraham et al. 1999). Recent ultra-deep X-ray surveys with Chandra have extended such results to fainter fluxes and harder X-ray energies (cf. Giacconi et al. 2001a, 2001b; Brandt et al. 2001; Hornschemeier et al. 2001; Mushotzky et al. 2000; Tozzi et al. 2001). Further evidence of a connection between AGN and galaxy evolution has been provided by the strong correlation between black hole mass and host

¹Based on observations made with the NASA/ESA Hubble Space Telescope, which is operated by the Association of Universities for Research in Astronomy, Inc., under NASA contract NAS 5-26555.

galaxy bulge velocity dispersion (Gebhardt et al. 2000; Ferrarese & Merritt 2000). However, the fundamental question of whether nuclear activity drives galaxy evolution, or vice versa, still remains open, and can only be addressed by obtaining high-resolution multi-wavelength observations of AGN *and* their hosts over a wide range of redshifts. The combination of *HST* and Chandra provides a unique opportunity to address these issues by first detecting distant AGN at X-ray energies, and subsequently obtaining high-resolution *HST* images of their host galaxy morphologies and environments.

In our first paper in this series (Schreier et al 2001, hereafter Paper I), we presented preliminary results from our program using the *HST* Wide Field Planetary Camera 2 (WFPC2) to image three regions in the Chandra Deep Field South (hereafter CDFS; Giacconi et al. 2001a). The analysis in that paper was based on the X-ray catalog and results from the first 300 ksec Chandra exposure (Tozzi et al. 2001).

In the present paper, we extend our discussion to the full 1 Msec X-ray dataset (Giacconi et al. 2001b). This provides a well-defined X-ray flux limited sample of objects that have optical counterparts observed with *HST*. We also present a more detailed discussion of our *HST*/WFPC2 observing strategy and analysis. In Section 2 we describe the observational strategy used with *HST*, in Section 3 we discuss the techniques used to reduce the data, in Section 4 we present the results from the observations, and in Section 5 we present a discussion of the implications of the various optical properties of the X-ray sources. Throughout this paper we adopt a cosmology with $\Omega_M = 0.3$, $\Omega_\Lambda = 0.7$, and $H_0 = 70 \text{ km s}^{-1} \text{ Mpc}^{-1}$.

2. Observing Strategy

The CDFS is centered at R.A. 03 32 28, Dec. $-27^{\circ} 48' 30''$ (J2000), with deep X-ray data covering an area $\sim 0.1 \text{ deg}^2$ (Giacconi et al. 2001a, 2001b). We used *HST*/WFPC2 to observe three regions within the CDFS, during 22 – 27 July 2000. Each of the three regions was observed for a total of five orbits, comprising ~ 2 orbits in the F606W filter and ~ 3 orbits in F814W. These two filters provide an optimal combination of high throughput, wide bandwidth and minimal spectral overlap, with well characterized photometric accuracy; the spectral coverage is continuous between $\sim 5000 - 9500 \text{ \AA}$, with a small overlap between the filters at $\sim 7200 \text{ \AA}$. Thereby these observations were specifically designed to yield good sensitivity to the color gradients and other morphological features that we expected to observe in the moderate-redshift galaxies in these fields (cf. Williams et al. 1996; Casertano et al. 2000). We chose a somewhat shorter exposure time for the F606W filter due to its higher overall throughput, thereby aiming to match our sensitivity to isophotal features on comparable spatial scales in both bands. In Table 1 we present a summary of the field coordinates

(specified as the location of the WFALL-FIX aperture reference position on WFPC2, which we used to obtain the observations), as well as the total exposure times and position angle of the +V3 axis of the telescope.

Several instrumental issues need to be addressed when observing with *HST*/WFPC2; these include the removal of cosmic rays, the presence of hot pixels and other detector artifacts, and the fact that the *HST* point spread function (PSF) is substantially undersampled by the $\sim 0''.1$ pixels in the three WF cameras (WF2, WF3 and WF4). We therefore obtained the observations in each filter using the “dither” mode, which involves offsetting the telescope by small increments to move the sources around the detector. We restricted the offsets to a maximum of $\lesssim 0''.75$ along each axis (corresponding to a total of 7.5 WF pixels). The use of larger shifts would have improved the cosmetic appearance of the final combined dataset, particularly by increasing the counts in the inter-chip gaps between the cameras. However, the $\sim 2\%$ geometric distortion present across each camera introduces increasingly significant non-uniform subsampling across the chip for offsets much larger than ~ 10 pixels. Since our primary objective was to obtain consistent sub-sampling across each chip, we therefore used the minimal offsets.

We employed a 4-point parallelogram dither pattern, in which the telescope was moved in steps of integral plus 1/2-pixel increments along both axes of the detector. The integral pixel shifts mitigate the effect of bad pixels, while the additional 1/2-pixel increments allow subsampling of the PSF. The ratio of pixel scales between the PC and the three WF cameras is ~ 0.45 , thus an offset of $0''.25$ corresponds to a 2.5-pixel shift in each of the three WF cameras, and a 5.5-pixel shift in the PC. The 4-point parallelogram dither pattern is therefore designed so that sources are optimally subsampled by all 4 quadrants of a pixel. We changed filters at each dither location, to minimize the number of offsets that the telescope was required to perform and also to reduce overhead. At each of the four dither locations we further obtained two exposures to improve removal of cosmic rays, as well as providing some redundancy to ensure that subsampling was achieved with at least one exposure in each of the 4 pixel quadrants, for most pixels across each chip. The multiple dithered exposures also reduce photometric errors due to flatfielding uncertainties.

In Table 2 we show the fractional pixel shifts in all 4 cameras, for each of the offsets. The dither offsets were specified in the POS TARG reference frame of the WFALL-FIX aperture of WFPC2, and therefore indicate the direction of motion of the field along the X and Y axes of the WF3 detector. The orientation of the shifts for the other cameras rotates, corresponding to the 90 degree rotational differences between the reference frames of the various chips.

In Figure 1 we show the offsets that were achieved for each of the three fields. Since

each field was observed for five contiguous orbits, a full guide star acquisition was only required at the start of each set of five orbits, while a re-acquisition was carried out at the start of each of the subsequent four orbits. For each of the three fields the observations were obtained in FINE LOCK mode, with successful acquisition of both guide stars. This permitted accurate offsetting and tracking during each set of five orbits. We measured an overall offsetting precision of ~ 10 mas r.m.s. when comparing the actual offsets with those that were commanded to the telescope. This translates to a fractional pixel positioning accuracy of ~ 0.1 pixel r.m.s. on each of the three WF chips, sufficient for our desired $\sim 1/2$ -pixel subsampling. The corresponding fractional pixel offset r.m.s. is larger on the PC camera due to its smaller pixel size, but this is mitigated by the fact that the PC pixels provide much better sampling of the PSF. Figure 1 confirms that the WF fractional pixel offsets generally lie within their respective pixel quadrants.

In Table 3 we present a summary of the observations, showing how the exposures in each filter were divided in terms of their dither pattern location. Some asymmetries in the exposure times at the different dither locations had to be introduced as a result of dividing four dither positions into five orbits, along with our requirement for obtaining a longer overall exposure time in F814W than F606W. However, we aimed to maintain exposure times that were as uniform as possible at each dither location. Thus the F814W exposure times varied between 600 – 800 s with a mean of 725 s, and the F606W exposures varied between 400 – 700 s with a mean of 463 s. This variation does not significantly compromise the statistical noise properties of the final images.

3. Data Reduction and Analysis Procedures

3.1. Pipeline Processing

The observations were initially processed with the standard pipeline calibration, at the point when they were retrieved from the HST Data Archive. This procedure consists of the following steps: masking bad pixels; analog-to-digital conversion; subtraction of the mean bias level; subtraction of the “superbias” image; subtraction of the “superdark” image (scaled according to the darktime of the observation); and multiplying by the flat field reference image for the appropriate filter. These standard procedures are documented in further detail in the HST Data Handbook V3 (Voit et al. 1997). After the data had been retrieved, they were recalibrated a few weeks later when the most up-to-date dark calibration reference files for the time of the observation became available.

3.2. Dithered Image Registration

After calibration, the images were processed using tasks in the IRAF/STSDAS *dither* package. The steps outlined in this section are similar to those used recently for the *HST*/WFPC2 observations of the HDF-S (Casertano et al. 2000), and also described in substantially more detail in the *HST* Dither Handbook (Koekemoer et al. 2000). Here we present a summary of the steps involved, and further details can be obtained by consulting these references.

The first step in this procedure involved removal of the sky background from each of the separate chips, using the task *sky* to bin the pixel fluxes into a histogram and calculate the mean background based on the width of the histogram distribution about its peak value. After sky subtraction, new pixel flux histograms were constructed to verify that the peak of the histogram distribution was now centered at zero for each chip.

We chose to use cross-correlation to calculate the relative offsets between images, since the F606W and F814W filter images of all three fields generally contained a sufficient number of objects bright enough to enable successful cross-correlation. The results from the cross-correlation were later verified by examining the jitter files for each observation retrieved from the *HST* Data Archive, and this generally revealed good overall agreement between the two methods (better than 10 mas).

To prepare the images for cross-correlation, the task *precor* was run on each chip. This task essentially filters the image, producing an output image that has flux in pixels only for sources having a given number of adjacent pixels above some specified value. This strategy allowed effective removal of most cosmic rays, by setting the required number of adjacent pixels sufficiently high. In the output image, blank regions and very faint objects were set to zero, in order to avoid adding noise to the cross-correlation.

Next, the task *offsets* was run, which makes use of the program *crosscor* to perform the cross-correlation. Each dither location contained 8 exposures for each of the two filters. The first of the 8 images was defined as the reference image, and *crosscor* then produced cross-correlation images for the other pointings relative to this image.

The task *shiftfind* was then run on the output cross-correlation images from *crosscor*, fitting a two-dimensional Gaussian to the central cross-correlation peak and yielding as output the x and y pixel location of the peak, together with their $1-\sigma$ uncertainties. Finally, the task *avshift* was run on the shifts of all 4 WFPC2 chips, using known information about the geometric relationships between the chips to average the shifts that were obtained independently for each chip, thereby producing a final improved value of the x,y shift of each WFPC2 pointing in the series of 8 images (these are the shifts displayed in Figure 1).

3.3. Cosmic Ray Rejection and Image Combination

After determining the shifts, the next steps involved combining the images and simultaneously carrying out cosmic ray rejection. To do this, we made use of a new capability of the *drizzle* software (Fruchter & Hook 2001), which permits direct removal of cosmic rays from individual images while at the same time performing the steps involved in combining them. We adopted an output image scale of 0.5 input WF pixels, motivated by the general success of our observational strategy in achieving half-pixel subsampling across all three WF cameras. While we obtained two images at each of the 4 dither positions, this was primarily intended to ensure redundancy in the subsampling; any attempt to remove cosmic rays by simply combining the two images would not result in optimal cosmic ray removal. Therefore we adopted a strategy of treating all 8 images separately in the cosmic ray removal process outlined here.

To create the cosmic ray masks, we first ran *drizzle* on each input image, using the offsets determined previously to shift them all onto separate output images having a common alignment. These images were then combined using a robust median rejection technique to remove all the cosmic rays, producing a somewhat noisy but clean image containing only real astronomical sources. This image was then transformed back onto the original frame of each input image, using the task *blot*, which essentially reverses the shifts that were applied by *drizzle*. The tasks *deriv* and *driz_cr* were then run on these images, thereby creating a final mask for each input image that contained all the cosmic rays, bad pixels, and other defects.

After creating the masks, the final step involved running *drizzle* once more on the input images, using the same shifts, but with the difference being that all the input images were “drizzled” onto a single output image, and also making use of the mask images to prevent cosmic rays and other defects from propagating onto the output image. The *drizzle* program also creates a corresponding “weight” image, representing the relative contribution of input pixels to each output pixel. We shrunk the footprint of the input pixels by a factor of 0.7 (specified by the *drizzle* parameter *pixfrac*), thereby improving the resolution of the output image by reducing the overall scale with which the output pixels are convolved, while still retaining sufficiently uniform sampling of the input image plane by the output pixel grid. More detailed discussions of these effects are presented in Koekemoer et al. (2000) and Fruchter & Hook (2001). We also created another set of images with *pixfrac* set to 1, which yielded somewhat lower resolution but improved weighted image statistics for object detection and photometry. These images were used to carry out the source detection described in the next section, while the higher resolution images with *pixfrac* set to 0.7 were subsequently used to examine the detailed morphology of the detected X-ray sources,

as presented in this paper.

3.4. Optical Identification of the X-ray Sources

We first created a detection image for each WFPC2 field by adding the F606W and F814W images, and then extracted objects using the SExtractor program. The measured count-rates were converted to the *HST*/WFPC2 ABMAG photometric system using the best available information (cf. *HST*/WFPC2 Instrument Handbook, V.5, 2000). Our source detection and extraction procedures are described in Paper I. In a forthcoming paper (Grogin et al. 2001, in preparation) we will describe in more detail our photometric procedures, including radial surface brightness photometry and profile fitting.

In Figure 3 we present greyscale images of the three fields, made by combining the F606W and F814W datasets. We also overlay the locations of all the X-ray sources in the 1 Msec catalog that are within the field of view of our WFPC2 images. Our three WFPC2 fields contain a total of 40 X-ray sources listed in the 1 Msec Chandra catalog, with 12 – 15 X-ray sources per field.

We registered each of the three WFPC2 fields independently to the *CXO* reference frame by subtracting the error-weighted median offset of the nearest *HST*/WFPC2 optical counterpart to each *CXO* source. The overall offset is different for each of the three fields since different guide stars were used — the general size of the offsets ($\sim 1''$) is consistent with the uncertainties inherent in the *HST* guide star catalog, as well as additional astrometric uncertainties present in the Chandra image.

After registering the frames by removing the overall offsets, we next examined the positional offset between each *CXO* source position and the location of the nearest *HST* source. The mean offset between the X-ray and nearest optical source was found to be $0''.33$ in right ascension and $0''.38$ in declination. When we examined the distribution of positional offsets in right ascension and declination combined, we found a $1-\sigma$ r.m.s. deviation of $0''.5$, which is consistent with the general *CXO* positional uncertainties quoted by Tozzi et al. (2001), particularly given that the *CXO* PSF becomes substantially degraded at the locations of some of our WFPC2 fields, away from the CDFS field center. In Figure 2(a) we show the positional offsets between the X-ray sources and the nearest detected optical counterparts, for each X-ray source, and in Figure 2(b) we show the magnitude of the offset as a function of off-axis angle in the Chandra ACIS-I image. The scatter in the offsets remains approximately constant and does not show any strong increase at larger off-axis angles. We found that 37 of the 40 X-ray catalog sources have an optical counterpart detected within our

3σ positional tolerance from the X-ray location. We note that in some cases, more than one optical identification is located within $0''.5$ of the X-ray source, hence there remains a formal statistical uncertainty in these cases about which optical source is the true counterpart. However, in these cases, a comparison between the X-ray and optical image generally reveals that the X-ray contours are well centered on a single object, as we discuss further in Section 4 where we present the X-ray overlays on the optical images.

The remaining three X-ray sources are more than $2''$ away (i.e., $\gtrsim 4\sigma$) from the nearest *HST*/WFPC2 object above our detection threshold. All three of these sources are on the PC and have 3σ detection limits of $F606W \geq 26.9$ and $F814W \geq 26.4$, based on $0''.5$ -radius apertures centered on the CXO coordinates. We note, however, that the detection limits on the PC are shallower than on the WF chips, primarily resulting from the increased read-noise due to the fact that there is a higher number of the smaller PC pixels per unit area on the sky. When we examine the fluxes of our remaining sample of 37 objects, we find that 35 of these (94.6%) would still have been detectable by the PC chip. Thus, for our total sample of 40 sources, the detection efficiency of the PC would be 87.5%, which is not statistically different from the 94.6% efficiency previously inferred (given the sample size of 40 sources). Since the PC field of view covers only $\sim 6\%$ of our total area, we consider it somewhat unlikely that the three non-detections on the PC could form part of a completely different population that is much fainter than any of the other sources that are detected on the WF chips.

To explore this issue further, however, we also examine the X-ray properties of the three undetected sources, as compared with the rest of the sources. Their average flux is 2.14×10^{-16} ergs s^{-1} and 1.32×10^{-15} ergs s^{-1} in the soft and hard band respectively. Of the optically identified sources, 19 have total X-ray fluxes greater than this, while 18 have fainter X-ray fluxes, thus the average flux of the three optically undetected sources lies near the median of the X-ray flux distribution. Of the 18 optical identifications that have fainter X-ray flux, 2 would not have been detected had they landed on the PC chip. Moreover, when we examine the constraints on the X-ray/optical flux ratios of the three undetected sources, we find that the lower limits on this ratio are not inconsistent with the typical values for the remainder of the sources, as can be seen by examining the X-ray fluxes and optical magnitudes in Table 4. Thus, although we cannot completely rule out the possibility that these three objects may have a much higher X-ray/optical ratio than the other sources in our sample, we consider it more plausible that they would likely have been detected had they fallen on the WF chips instead of the PC, and that these sources may thus form part of the same population as some of the optically faint sources that are detected on the WF chips.

4. Results

4.1. Optical Properties of the X-Ray Sources

Figure 4 shows $20'' \times 20''$ *HST* subimages (derived from the combined F606W and F814W datasets), centered on the coordinates of each of the 40 *CXO* sources from the 1 Msec catalog (Giacconi et al. 2001b) that are located within our WFPC2 fields, with contours overlaid from the 1 Msec 0.5 – 7 keV X-ray image. It can be seen that, in general, the agreement between the centroid of the *CXO* contours and the peak of the optical emission is remarkably good. This is the case not only for optically bright, unresolved objects but also for many of the fainter objects as well as those that are extended in the optical images but do not display a dominant nuclear component. We also note that the X-ray contours in general are unresolved or display only marginal spatial extent; the variation in the structure of the X-ray contours is predominantly due to changes in the *CXO* PSF across the fields of view covered by our *HST* observations (Giacconi et al. 2001b).

In Table 4, we list the F606W and F814W magnitudes (or 3σ upper limits) for all 40 *CXO* sources located in our WFPC2 fields, as measured from our SExtractor photometry. We also tabulate the *CXO* fluxes in the soft (0.5 – 2 keV) and hard (2 – 10 keV) bands (columns F_{XS} and F_{XH} respectively), together with the X-ray hardness ratio values HR reported by Giacconi et al. (2001b) (ranging from $HR = -1$ for sources detected only in the soft band, to $HR = +1$ for sources detected only in the hard band).

In Table 4 we also present information about the optical morphology of the *HST* counterparts, indicating whether or not the source is resolved and if so, what galaxy class it appears to be. We found that the SExtractor star/galaxy separation was reliable to F606W ~ 25.5 , substantially fainter than the majority of the counterparts to the *CXO* sources. Thirty of the 37 optical counterparts to the X-ray sources are clearly resolved, of which 25 were sufficiently extended to permit detailed examination and classification as elliptical, spiral or irregular galaxies. The remaining five were too faint and/or not sufficiently extended to permit reliable classification, thus we list them as “indeterminate” morphology in Table 4.

4.2. Color-Magnitude Properties of the X-ray Optical Counterparts

In Figure 5 we plot the F814W magnitudes and F606W – F814W colors of all the sources in our SExtractor catalog (Grogin et al. 2001, in preparation). The field galaxies (unassociated with any X-ray source) are plotted as small dots; the 37 optical counterparts of the *CXO* sources are plotted with larger symbols indicating their optical morphology

and X-ray properties. Circles represent resolved early-type galaxies (types S0 and earlier); squares are resolved late-type spirals / irregulars (types Sa and later); stars represent clearly unresolved sources; and triangles are objects of indeterminate morphology. The sizes of the symbols correspond to total X-ray flux in the $0.5 - 10$ keV band, with size being proportional to higher flux. The symbols are also shaded with a greyscale intensity according to their hardness ratio: soft sources are shown with a light shading, while hard sources are darker.

With our increased number statistics, we are able to confirm the dichotomy (reported in Paper I) in the color magnitude distribution of the optical counterparts of the X-ray sources: a brighter group with $F814W \sim 18 - 24$, and a fainter group with $F814W \gtrsim 24$. The fainter group is consistent in its color distribution with the field galaxy population. The other group is both significantly brighter and significantly redder, on average, than the population of field sources.

We overlay predicted templates for elliptical, spiral, and irregular / starburst galaxies, as well as Type 1 AGN (as in Paper I; see also Williams et al. 1996). These tracks show that the population of bright, extended X-ray sources should consist of a mix of morphological types at low to moderate redshifts, including Type 1 AGN, while the optically fainter X-ray sources are likely too blue to be early-type galaxies.

In order to further explore this apparent dichotomy in color-magnitude space, we present in Figure 6 a montage of all the WFPC2 images of the X-ray sources, with blue representing $F606W$, red representing $F814W$, and green a mean image of the two. The overall structure of this figure is schematically similar to Figure 5: the vertical panels are arranged in order of decreasing apparent magnitude toward the bottom, with redder objects toward the right; the horizontal panels at the bottom represent the faint group (most of which are blue) together with the three X-ray sources that have no optical counterparts in the *HST* images. The sources are divided into the following groups, according to their distribution in the color-magnitude diagram presented in Figure 5:

- Bright ($F814W \lesssim 24$); blue ($F606W - F814W \lesssim 0.7$): These sources all contain an unresolved nucleus, contributing a substantial portion of the total flux of the object – they are likely Type 1 AGN, and this is confirmed by the optical spectra as well as the X-ray and optical luminosities of those objects for which spectra are available so far. More specifically, we have so far obtained spectra for 4 of these objects (CDFS ID's 39, 60, 62, and 63), and all of them can be definitively classified as Type 1 AGN on the basis of their spectra. More detailed discussions concerning the analysis and interpretation of the spectroscopic data will be presented in a forthcoming paper (Hasinger et al. 2001, in preparation).

- Bright ($F814W \lesssim 24$); intermediate color ($F606W - F814W \sim 0.7 - 1.2$): These objects are all spatially resolved by our *HST* observations, and we are able to classify them morphologically as either elliptical, S0, or spiral galaxies. The fluxes of these objects are dominated by their host galaxies rather than by a bright, unresolved nucleus; a faint nucleus may however be present in a number of these objects. We further divide these objects into soft (left-hand column) and hard (right-hand column); there appears to be no discernible systematic difference between these classes in terms of either the host galaxy morphological type, the prominence of the central nucleus (or lack thereof), or apparent magnitude. However, these sources are in general harder than the bright blue population.
- Bright ($F814W \lesssim 24$); red ($F606W - F814W \gtrsim 1.2$): The objects in this class are also spatially resolved in our data, and appear to consist predominantly of early-type galaxies. Two of them display some hint of spiral structure, but their overall color is still much redder than the more spatially extended spirals in the bluer populations; this may be due either to a higher redshift or intrinsically large amounts of dust. We again divide these objects into soft (left-hand column) and hard (right-hand column), and once more there is no clear morphological difference between the two types.
- Faint ($F814W \gtrsim 24$): These objects are plotted as horizontal panels near the bottom of the figure, divided into hard (top panel) and soft (bottom panel). Although these objects are small, they are all nonetheless resolved by our *HST* observations — there is no indication of any unresolved nuclear component contributing a substantial part of the flux. Thus we are able to rule out the possibility that these are distant Type 1 AGN; furthermore Type 1 AGN at these optical flux levels would have been too faint to be detected in the current Chandra dataset. Instead, these objects appear to be drawn from the same population as the rest of the faint blue galaxy population. We draw attention to one exceptional object, which is much redder than the others and presumably belongs to a different class; we will return to a more detailed discussion of this source in the next section.

For completeness, we also show the three non-detections at the bottom of Figure 6). These were all on the PC chip where the detection threshold is shallower than on the WF chips, as we have discussed earlier in Section 3.4.

5. Discussion: Optically Bright and Faint Sources – Two Distinct Populations

The single most prominent result from this study is the clear separation of the X-ray sources into two apparently distinct populations in color-magnitude space. Our earlier study, based on the 300 ks data (Paper I) suggested this but contained only 5 sources in the faint population. By extending our study to the full sample of X-ray sources from the 1 Msec catalog, this result has now been shown to remain robust, with 10 faint sources and 27 in the brighter group.

To quantitatively examine the nature of these two populations, we used published SEDs and luminosity functions for various classes of galaxies to calculate the expected numbers of objects detected in our study (as described in Paper I, and also to be addressed in more detail in a forthcoming paper, Koekemoer et al. 2001, in preparation). In Figure 7, we present a histogram of the F814W magnitude distribution of the X-ray sources, together with the predicted distributions for ellipticals, spirals, starbursts, and AGN in the area of sky corresponding to our three WFPC2 fields, and applying the appropriate X-ray detection thresholds. We have not adjusted any free parameters in the models when calculating the distributions, which could of course improve the normalizations somewhat — rather, we have simply adopted the published luminosity functions as representative of each of the galaxy classes that we detect. Specifically, the distribution of each galaxy class is simply the result of calculating the number counts of that type of object based on the assumed SED, luminosity function and evolution (which produces a distribution that rises steeply toward fainter magnitudes), and applying the X-ray flux limits corresponding to the 1 Msec survey. This begins to cut off the rising distribution at the corresponding F814W magnitude, which to first order is characteristic of the F_X/F_{opt} ratio of each class of object; second-order effects such as redshift K-correction produce a tail toward fainter magnitudes. It is thus encouraging that the models agree with the observed distributions to this level of detail.

The models in Figure 7 suggest that the majority of the X-ray optical counterparts are expected to be relatively bright, comprising a wide range of galaxy types including ellipticals, spirals, starbursts, and AGN, and this is completely consistent with what we observe. We note that many of the objects classified as “spirals” (from the SEDs published by Schmitt et al. 1997) may in fact harbor low-luminosity, X-ray emitting AGN, as suggested by Ho, Filippenko & Sargent (1995); their X-ray luminosities are likely to be at least one to two orders of magnitude below that of the objects classified by Schmitt et al. (1997) as “Seyferts”. Much more interesting, however, is the realization that the population of fainter, blue X-ray emitting sources apparently consist predominantly of Type 2 AGN located at higher redshifts ($z \sim 1 - 2$). This interpretation is supported independently from a study recently completed by Alexander et al. (2001) for the CDF-N, and here we further explore some of

its implications.

The lack of Type 1 AGN in the population of optically faint X-ray sources is primarily a consequence of the F_X/F_{opt} ratio, and can be understood as follows. If we consider Type 1 and Type 2 AGN of comparable X-ray luminosity, located in similar host galaxies at redshifts $z \gtrsim 1$, then the detected X-ray emission from both types of objects would be comparable — although some of the softer X-rays from the Type 2 AGN would be absorbed by the obscuring torus, the majority of the X-rays harder than a few keV are able to penetrate, and at higher redshifts these X-rays are shifted toward the soft end, thereby producing comparable total X-ray fluxes for Type 1 and Type 2 AGN in the 0.5 – 10 keV Chandra bandpass. Thus, we can consider the hard X-ray emission to be approximately isotropic. However, the total optical emission from a source containing a Type 1 nucleus is brighter than that of a comparable Type 2 by a few magnitudes, because of the dominant contribution from the unobscured Type 1 nucleus. Hence, Type 1 AGN detected near the X-ray sensitivity threshold of the 1 Msec survey cannot be optically fainter than $F814W \sim 22 - 24$. However, Type 2 AGN detected near the same X-ray threshold can be considerably fainter in the optical since the nuclear emission is obscured, and only the host galaxy contributes to the observed optical emission. If the Type 2 AGN is of only moderate luminosity, as expected on the basis of the X-ray fluxes presented here, then it is likely located in a late-type galaxy, which at $z \sim 1 - 2$ would become optically indistinguishable from the faint blue galaxy population. We note that more distant, or less luminous, Type 1 AGN may of course still be present among the faint blue galaxy population ($F814W \gtrsim 24$). They would be too faint at X-ray energies to be detected at the depth of the 1 Msec survey, but in this scenario they should become visible in deeper Chandra observations, for example as currently planned for the CDF-N.

We can similarly rule out starbursts as a possible explanation for the faint blue X-ray population, once again based on the ratio of X-ray to optical emission which is substantially lower for starbursts than for Type 2 AGN. Given the X-ray sensitivity thresholds of the 1 Msec catalog, starbursts detected in this survey are not likely to be optically fainter than $F814W \sim 23$ at most, since any fainter (more distant) starbursts would not be detectable in the X-rays. The same arguments apply to ellipticals and spirals without AGN — those that are at sufficiently high redshift to be in the part of the diagram with $F814W \gtrsim 24$ would not be detected in the 1 Msec survey. These arguments are supported quantitatively by the comparison between the models and the observed number distributions of objects in Figure 7, which imply that the predominant population of faint blue X-ray sources has to be low to moderate luminosity Type 2 AGN, located at redshifts $z \sim 1 - 2$.

We finally describe one object of particular interest in the faint population, CDFS ID #515 (J033232.2–274652), located on the WF4 chip in the CDFS1 field. This object is at

least one magnitude redder than the rest of the faint blue population; it is undetected in F606W down to a 3σ limit of 27.9, thus its color is $F606W - F814W \gtrsim 1.4$. If this object is a Type 2 AGN then its host galaxy is early-type or excessively dust-rich. However, we cannot rule out the possibility that this object could be an highly reddened QSO — i.e., an AGN of much higher intrinsic luminosity than the other active nuclei discussed in this section, but reddened by substantial amounts of dust. The fact that we only observe one of these in our sample could support the interpretation of a higher intrinsic luminosity, thus a lower space density, for this object, although other explanations may also be possible. It is expected that deep spectroscopic observations would yield more definitive information about this object.

6. Conclusions

We have presented *HST*/WFPC2 observations of an X-ray flux limited sample of 40 sources from the 1 Msec CDFS catalog, thereby completing our earlier study which had been based on the 300 ks X-ray catalog. We find that 37 of the X-ray sources in our WFPC2 fields have apparent optical counterparts within ~ 1 arcsec; the three non-detections were all on the PC chip where the detection threshold is shallower than on the WF chips, but their non-detection is not inconsistent with the optical/X-ray fluxes of the faint sources detected on the WF chips at comparable magnitudes. In fact, had they fallen on the WF chips we find that they would most likely have been detected; since all 37 sources on the WF chips are detected, we conclude that *HST*/WFPC2 observations to this depth are potentially capable of detecting all the sources from the 1 Msec catalog.

The principal result from this work, which had been suggested with a small number of sources in Paper I and now confirmed with a substantially increased sample in the present paper, is the realization that the optical counterparts of the 1 Msec X-ray sources consist of two distinct populations: a brighter population, with $F814W \sim 18 - 24$; and a fainter population, with $F814W \gtrsim 24$. The brighter population is both significantly brighter and significantly redder on average than the population of field sources. The fainter population, on the other hand, is consistent in its magnitude and color distribution with the majority of the faint blue field galaxy population.

Specifically, we have shown that this optically faint blue group is likely to consist predominantly of low to moderate luminosity Type 2 AGN at reasonably high redshifts for this class of object (at least $z \sim 1 - 2$). Their optical properties would be dominated by their hosts, most probably late-type galaxies. These Type 2 AGN are the only population of sources with a sufficiently high ratio of X-ray to optical emission to be detectable in the

1 Msec catalog while simultaneously displaying such faint optical magnitudes; other classes of objects (including normal galaxies, starbursts, and unobscured AGN) are observed at brighter optical magnitudes but would not be detectable in the 1 Msec catalog at these faint magnitude levels.

We have also discovered a faint, red X-ray source that is undetected in F606W and has an F606W – F814W color at least 1 magnitude redder than the rest of the faint X-ray emitting population. This object may also be a Type 2 AGN of comparable luminosity to the others but located in a redder host galaxy, for example an early-type galaxy or one that contains excessive amounts of dust. However, this object may also be an example of a class of much more luminous (hence more sparse) reddened, dusty QSOs located at higher redshift. Deep spectroscopy should yield more clues about its nature.

In conclusion, we can state that the combination of deep Msec-level X-ray surveys together with the unprecedented spatial resolution of *HST*, are for the first time providing us with the ability to probe the faint end of the obscured AGN luminosity function at cosmologically interesting redshifts. This is supported by the relatively robust agreement between our observations and models based on luminosity functions of AGN and normal galaxies. These results show that we now have the capability to investigate in detail the morphological properties of these sources and classify them accordingly. Our *HST* observations cover only 7.5% of the full-depth 1 Msec CDFS area (Giacconi et al. 2001b), thus there is clearly an enormous potential for further observations to increase both the sample size and the depth at which these objects are studied. Combined with deep spectroscopy on 8m-class telescopes and studies at other wavebands (including, for example, mid- to far-IR imaging with SIRTF), such samples will eventually be able to probe up to and beyond the expected peak in AGN density evolution at $z \sim 2$, as well as revealing their relationships to starbursts and other galaxy classes.

We gratefully acknowledge the award of *HST* Director’s Discretionary time in support of this project. We also acknowledge support for this work which was provided by NASA through GO grants GO-08809.01-A and GO-07267.01-A from the Space Telescope Science Institute, which is operated by AURA, Inc., under NASA Contract NAS 5-26555. We thank the referee for very useful suggestions that helped to improve this paper.

REFERENCES

Abraham, R. G., Ellis, R., Fabian, A., Tanvir, N., & Glazebrook, K. 1999, MNRAS, 303, 641

Alexander, D. M., Brandt, W. N., Hornschemeier, A. E., Garmire, G. P., Schneider, D. P., & Bauer, F. E. 2001, ApJ, in press (astroph/0107450)

Bertin, E. & Arnouts, S. 1996, A&AS, 117, 393

Biretta, J. A. et al. 2000, WFPC2 Instrument Handbook, Version 5.0 (Baltimore: STScI)

Brandt, W. N., Hornschemeier, A. E., Alexander, D. M., Garmire, G. P., Schneider, D. P., Broos, P. S., Townsley, L. K., Bautz, M. W., Feigelson, E. D., & Griffiths, R. E. 2001, AJ 122, 1

Boyle, B. J., Shanks, T., Croom, S. M., Smith, R. J., Miller, L., Loaring, N., & Heymans, C. 2000, MNRAS, 317, 1014

Casertano, S., de Mello, D., Dickinson, M., Ferguson, H. C., Fruchter, A. S., Gonzalez-Lopezlira, R. A., Heyer, I., Hook, R. N., Levay, Z., Lucas, R. A., Mack, J., Makidon, R. B., Mutchler, M., Smith, T. E., Stiavelli, M., Wiggs, M. S., & Williams, R. E. 2000, AJ 120, 2747

Coleman, G. D., Wu, C.-C., & Weedman, D. W. 1980, ApJS, 43, 393

Cristiani, S. & Vio, R. 1990, A&A 227, 385

Della Ceca, R., Maccacaro, T., Rosati, P., & Braito, V. 2000, A&A 355, 121

Ferrarese, L. & Merritt, D. 2000, ApJ, 539, 9

Fruchter, A. S. & Hook, R. 2001, PASP, submitted

Gebhardt, K., Kormendy, J., Ho, L. C., Bender, R., Bower, G., Dressler, A., Faber, S. M., Filippenko, A. V., Green, R., Grillmair, C., Lauer, T. R., Magorrian, J., Pinkney, J., Richstone, D., & Tremaine, S. 2000, ApJ, 539, 13

Giacconi, R., Rosati, P., Tozzi, P., Nonino, M., Hasinger, G., Norman, C., Bergeron, J., Borgani, S., Gilli, R., Gilmozzi, R., & Zheng, W. 2001a, ApJ, in press (astro-ph/0007240)

Giacconi, R., Zirm, A., Wang, J. X., Rosati, P., Nonino, M., Tozzi, P., Gilli, R., Mainieri, V., Hasinger, G., Kewley, L., Bergeron, J., Borgani, S., Gilmozzi, R., Grogan, N., Koekemoer, A., Schreier, E., Zheng, W. & Norman, C. 2001b, ApJ, submitted

Grogan, N. A. et al. 2001, in preparation

Hasinger, G., Burg, R., Giacconi, R., Schmidt, M., Truemper, J., & Zamorani, G. 1998, A&A, 329, 482.

Hasinger, G., et al. 1999, in "Highlights in X-ray Astronomy", MPE report 272, 199 (astro-ph/9901103)

Hasinger, G., et al. 2001, in preparation

Hornschemeier, A. E., Brandt, W. N., Garmire, G. P., Schneider, D. P., Barger, A. J., Broos, P. S., Cowie, L. L., Townsley, L. K., Bautz, M. W., Burrows, D. N., Chartas, G., Feigelson, E. D., Griffiths, R. E., Lumb, D., Nousek, J. A., Ramsey, L. W., Sargent, W. L. W. 2001, *ApJ*, 554, 742

Koekemoer, A. M., Gonzaga, S., Fruchter, A., Biretta, J., Casertano, S., Hsu, J.-C., Lallo, M., Mutchler, M., & Hook, R. 2000, *The HST Dither Handbook* (Baltimore: STScI)

Koekemoer, A. M., et al. 2001, in preparation

Lilly, S., Schade, D., Ellis, R., Le Fevre, O., Brinchmann, J., Tresse, L., Abraham, R., Hammer, F., Crampton, D., Colless, M., Glazebrook, K., Mallen-Ornelas, G., & Broadhurst, T. 1998, *ApJ*, 500, 75

Loveday, J., Peterson, B. A., Efstathiou, G., & Maddox, S. J. 1992, *ApJ*, 390, 338

Magorrian, J., Tremaine, S., Richstone, D., Bender, R., Bower, G., Dressler, A., Faber, S. M., Gebhardt, K., Green, R., Grillmair, C., Kormendy, J., Lauer, T. 1998, *AJ*, 115, 2285

Maiolino, R., Salvati, M., Antonelli, L., Comastri, A., Fiore, F., Ghinassi, F., Gilli, R., La Franca, F., Mannucci, F., Risaliti, G., Thompson, D., & Vignali, C. 2000, *A&A*, 355, L47

Miyaji, T., Hasinger, G., & Schmidt, M. 2000, *A&A*, 353, 25

Mushotzky, R., Cowie, L. L., Barger, A. J., & Arnaud, K. A. 2000, *Nature*, 404, 459

Risaliti, G., Marconi, A., Maiolino, R., Salvati, M. & Severgnini, P. 2001, *A&A*, submitted (astro-ph/0102427)

Rosati, P., Tozzi, R., Giacconi, R., Gilli, R., Hasinger, G., Kewley, L., Mainieri, V., Nonino, M., Norman, C., Szokoly, G., Wang, J. X., Zirm, A., Bergeron, J., Borgani, S., Gilmozzi, R., Grogin, N., Koekemoer, A., Schreier, E., & Zheng, W. 2001, *ApJ*, submitted

Saunders, W., Rowan-Robinson, M., Lawrence, A., Efstathiou, G., Kaiser, N., Ellis, R. S. & Frenk, C.S. 1990, *MNRAS*, 242, 318

Schmidt, M., Giacconi, R., Hasinger, G., Truemper, J., & Zamorani, G. 1998, in "Highlights in X-ray Astronomy", MPE report 272

Schmitt, H. R., Kinney, A. L., Calzetti, D., & Storchi-Bergmann, T. 1997, *AJ* 114, 592

Schreier, E. J., Koekemoer, A. M., Grogin, N. A., Giacconi, R., Gilli, R., Kewley, L.; Norman, C., Hasinger, G., Rosati, P., Marconi, A., Salvati, M., & Tozzi, P. 2001, ApJ, submitted (astro-ph/0105271)

Tozzi, P., Rosati, P., Nonino, M., Bergeron, J., Borgani, S., Gilli, R., Gilmozzi, R., Hasinger, G., Grogin, N., Kewley, L., Koekemoer, A., Norman, C., Schreier, E., Shaver, P., Szokoly, G., Wang, J. X., Zheng, W., Zirm, A. & Giacconi, R. 2001, ApJ, submitted (astro-ph/0103014)

Urry, C. M. & Padovani, P. 1995, PASP, 107, 803

Voit et al. 1997, HST Data Handbook (Baltimore: STScI)

Whitmore, B., Heyer, I., & Casertano, S. 1999, PASP, 111, 1559

Williams, R. E., Blacker, B., Dickinson, M., Dixon, W. V., Ferguson, H. C., Fruchter, A. S., Giavalisco, M., Gilliland, R. L., Heyer, I., Katsanis, R., Levay, Z., Lucas, R. A., McElroy, D. B., Petro, L., Postman, M., Adorf, H.-M., & Hook, R. 1996, AJ 112, 1335

Table 1. Observed Fields

Field	R.A. (J2000)	Dec. (J2000)	F606W Exp. Time (s)	F814W Exp. Time (s)	+V3 Orientation (degrees)
CDFS1	03 32 28.80	−27 45 53.0	3700	5800	65
CDFS2	03 32 07.60	−27 46 35.0	3700	5800	65
CDFS3	03 32 12.70	−27 43 02.0	3700	5800	65

Table 2. Dither Strategy

Dither Offset (arcseconds)	PC (pixels)	WF2 (pixels)	WF3 (pixels)	WF4 (pixels)
0''.00, 0''.00	0, 0	0, 0	0, 0	0, 0
0''.50, 0''.25	−11.0, −5.5	−2.5, 5.0	5.0, 2.5	2.5, −5.0
0''.75, 0''.75	−16.5, −16.5	−7.5, 7.5	7.5, 7.5	7.5, −7.5
0''.25, 0''.50	−5.5, −11.0	−5.0, 2.5	2.5, 5.0	5.0, −2.5

Table 3. *HST*/WFPC2 Observation Log

Dither Offset (arcseconds)	WFPC2 Filter	Exp. Time (s)	CDFS1 Start Time (UT)	CDFS2 Start Time (UT)	CDFS3 Start Time (UT)
0''.00, 0''.00	F814W	700	2000 Jul 22 19:14:15	2000 Jul 23 16:09:15	2000 Jul 27 19:56:15
0''.00, 0''.00	F814W	700	2000 Jul 22 19:31:15	2000 Jul 23 16:26:15	2000 Jul 27 20:13:15
0''.00, 0''.00	F606W	700	2000 Jul 22 19:48:15	2000 Jul 23 16:43:15	2000 Jul 27 20:30:15
0''.00, 0''.00	F606W	500	2000 Jul 22 20:48:15	2000 Jul 23 17:43:15	2000 Jul 27 21:28:15
0''.50, 0''.25	F814W	800	2000 Jul 22 21:02:15	2000 Jul 23 17:57:15	2000 Jul 27 21:42:15
0''.50, 0''.25	F814W	800	2000 Jul 22 21:21:15	2000 Jul 23 18:16:15	2000 Jul 27 22:01:15
0''.50, 0''.25	F606W	400	2000 Jul 22 22:25:15	2000 Jul 23 19:20:15	2000 Jul 27 23:05:15
0''.50, 0''.25	F606W	400	2000 Jul 22 22:34:15	2000 Jul 23 19:29:15	2000 Jul 27 23:14:15
0''.75, 0''.75	F814W	600	2000 Jul 22 22:46:15	2000 Jul 23 19:41:15	2000 Jul 27 23:26:15
0''.75, 0''.75	F814W	600	2000 Jul 22 22:59:15	2000 Jul 23 19:54:15	2000 Jul 27 23:39:15
0''.75, 0''.75	F606W	400	2000 Jul 23 00:05:15	2000 Jul 23 20:56:15	2000 Jul 28 00:43:15
0''.75, 0''.75	F606W	400	2000 Jul 23 00:14:15	2000 Jul 23 21:05:15	2000 Jul 28 00:52:15
0''.25, 0''.50	F606W	400	2000 Jul 23 00:26:15	2000 Jul 23 21:17:15	2000 Jul 28 01:04:15
0''.25, 0''.50	F606W	500	2000 Jul 23 00:35:15	2000 Jul 23 21:26:15	2000 Jul 28 01:13:15
0''.25, 0''.50	F814W	800	2000 Jul 23 01:47:15	2000 Jul 23 22:33:15	2000 Jul 28 02:22:15
0''.25, 0''.50	F814W	800	2000 Jul 23 02:06:15	2000 Jul 23 22:52:15	2000 Jul 28 02:41:15

Table 4. Properties of the WFPC2 counterparts to the 1 Msec CDFS X-ray sources

CDFS ID	IAU-Format Designation	$(\Delta\alpha, \Delta\delta)^a$ (arcsec)	F606W	F814W	$\log F_{X\text{S}}$ (cgs)	$\log F_{X\text{H}}$ (cgs)	HR	Optical Morphology
36	J033233.1–274548	(+0.02, –0.03)	22.61	21.63	–15.01	–14.54	–0.36	Spiral in CG
38	J033230.3–274505	(–0.01, –0.06)	22.30	21.79	–14.31	–14.05	–0.56	Unresolved
39	J033230.1–274530	(+0.02, –0.02)	21.45	21.36	–14.17	–13.81	–0.47	Unresolved
52	J033217.2–274304	(+0.15, –0.02)	21.66	20.81	–14.41	–14.13	–0.54	Elliptical
56	J033213.3–274241	(+0.39, –0.18)	20.85	20.00	–14.67	–13.77	+0.11	Ell., merger?
58	J033211.8–274629	(–0.05, –0.04)	26.05	25.32	–15.21	–14.73	–0.34	LSB Spiral
60	J033211.0–274415	(+0.34, +0.03)	22.50	21.96	–14.28	–13.94	–0.48	Unresolved
61	J033210.6–274309	(+0.27, +0.07)	24.98	23.05	–14.35	–13.96	–0.44	Unresolved
62	J033209.5–274807	(–0.13, –0.03)	20.98	20.55	–15.02	–14.27	–0.04	Unresolved
63	J033208.7–274735	(–0.05, +0.01)	19.28	18.73	–13.42	–13.10	–0.49	Unresolved
64	J033208.1–274658	(–0.04, –0.04)	25.39	25.17	–14.73	–14.23	–0.31	Spiral in group
66	J033203.7–274604	(+0.22, +0.08)	21.45	20.16	–15.29	–13.95	+0.56	S0
67	J033202.5–274601	(+0.29, –0.06)	24.81	23.62	–14.42	–13.99	–0.40	Elliptical
78	J033230.1–274524	(+0.01, +0.02)	23.11	22.28	–14.78	–14.50	–0.54	Unresolved
81	J033226.0–274515	(–0.05, –0.03)	26.56	26.24	–15.44	–15.05	–0.43	Indeterminate
83	J033215.0–274225	(+0.62, –0.63)	23.64	22.65	–15.07	–14.46	–0.22	Elliptical
86	J033233.9–274521	(–0.15, –0.38)	25.54	25.13	–15.93	–15.16	–0.04	LSB Irregular
89	J033208.3–274153	(+0.78, –0.44)	25.32	25.20	–15.37	–14.98	–0.44	Indeterminate
149	J033212.3–274621	(–0.10, +0.15)	23.86	22.55	–15.92	–15.03	+0.12	Spiral
155	J033208.0–274240	(+0.67, +0.06)	22.80	21.73	–15.84	–14.88	+0.17	Spiral
173	J033216.8–274327	(–0.18, –0.35)	22.97	22.01	–16.11	< –15.5	–1.00	Spiral
185	J033211.0–274343	(–0.29, –0.41)	22.52	21.47	–16.12	–15.19	+0.14	Spiral
224	J033228.8–274621	(+0.11, +0.10)	23.05	21.65	–15.62	< –15.5	–1.00	Elliptical
226 ^b	J033204.5–274644	...	>26.9	>26.4	–15.34	–14.93	–0.40	...
227 ^b	J033205.4–274644	...	>26.9	>26.4	–16.00	–14.66	+0.57	...
266	J033214.0–274249	(–0.15, –0.08)	22.43	21.36	< –16.5	–14.88	+1.00	Elliptical
515 ^c	J033232.2–274652	(+0.04, +0.02)	>27.9	26.41	–16.09	–14.90	+0.42	Indeterminate
518 ^b	J033226.9–274605	...	>26.9	>26.4	–16.08	–15.25	+0.03	...
532	J033214.2–274231	(–0.15, +0.28)	24.89	24.51	–15.86	–15.10	–0.05	Indeterminate
535	J033211.5–274650	(–0.15, –0.34)	22.81	21.74	–15.70	–14.90	+0.02	Elliptical
536	J033210.9–274235	(–0.29, +0.14)	20.27	19.34	–15.76	–15.17	–0.24	Elliptical
538	J033208.6–274649	(+0.04, –0.01)	19.82	18.94	–15.99	–15.11	+0.12	Spiral
560	J033206.3–274537	(+1.06, +0.37)	22.85	21.42	–15.93	< –15.5	–1.00	Spiral
563	J033231.5–274624	(–0.05, +0.55)	23.62	23.12	–16.22	< –15.5	–1.00	Spiral / Irr.
593	J033214.8–274403	(+1.32, +0.62)	26.42	25.52	–16.08	< –15.5	–1.00	LSB Irregular
594	J033209.8–274249	(–0.33, +0.87)	22.65	20.88	–15.48	< –15.5	–1.00	Elliptical
623	J033228.6–274659	(+0.73, –0.06)	26.96	26.63	–16.11	< –15.5	–1.00	Indeterminate
624	J033229.3–274708	(–0.21, +0.05)	22.61	21.06	–16.11	< –15.5	–1.00	Elliptical
626	J033209.5–274758	(+0.86, +0.84)	25.71	25.26	–16.05	< –15.5	–1.00	LSB Irregular
631	J033215.2–274335	(–0.36, –0.08)	25.26	23.85	–15.99	< –15.5	–1.00	Elliptical

^aJ2000 Right Ascension α and Declination δ offsets (HST –CXO), in arcsec.

^bNo counterpart within 2'' of CXO position; F606W, F814W mags are 3 σ upper limits for the PC chip.

^cThis object is detected in F814W on the WF4 chip with a magnitude F814W=26.41 (the limiting magnitude on the WF4 chip is 27.4); however it is not detected in F606W down to the 3 σ F606W limiting magnitude of 27.9.

Fig. 1.— Dither strategy employed in the *HST*/WFPC2 observations of the three fields in the CDFS. For each field, the observations were obtained using a parallelogram dither pattern specified in the POS TARG reference frame of the WFALL-FIX coordinate system (i.e., along the X,Y axes of the WF3 detector). The measured shifts for each field location are shown in the top panels, along with dashed lines indicating the commanded offsets. It can be seen that the r.m.s. positioning accuracy of the large-scale offsets is generally well within 10 mas, while drifts at each location, from one exposure to the next, are within 5 mas. The bottom panels display the shifts in terms of the fractional sub-pixel offsets of the three WF chips (WF2, WF3, WF4). Circles correspond to WF2, triangles to WF3 and squares to WF4. Open symbols are for the F606W images, and filled symbols correspond to F814W. For example, a source initially centered at the bottom-left quadrant of the pixel would move around to the other three quadrants as shown. These figures show that the dither offsets have generally been successful in achieving the desired 1/2-pixel subsampling along both the X and Y axes of the detectors.

Fig. 2.— (a) Offsets in right ascension and declination to the nearest HST optical counterpart, for each of the 40 X-ray sources in our three WFPC2 fields of view. The three open squares represent sources for which the offset is significantly larger than the 4σ statistical variation, and we thus do not consider these as positive identifications. The other 37 X-ray sources are all identified with optical counterparts, as discussed further in the text. (b) Offset as a function of off-axis angle on the Chandra ACIS-I chip. Our 3 WFPC2 fields cover a substantial range of off-axis angles; this plot shows that the scatter of positional offsets remains approximately the same and does not show a significant increase at larger off-axis angles.

Fig. 3.— *HST* greyscale images of each of the three WFPC2 fields in the CDFS, made by combining the F606W and F814W datasets. North is to the top and East is to the left. We also indicate the location of each of the X-ray sources from the 1 Msec Chandra catalog that are located within our WFPC2 field of view. The X-ray source identifications correspond to the nomenclature of Giacconi et al. (2001b). (a) This figure is for the CDFS1 field.

Fig. 3.— (b) As for Fig. 3a, but for the CDFS2 field.

Fig. 3.— (c) As for Fig. 3a, but for the CDFS3 field.

Fig. 4.— (a) *HST* greyscale images of each of the X-ray sources in the three CDFS WFPC2 fields, made by combining the F606W and F814W datasets. The X-ray contours from the smoothed 1 Msec Chandra data are overlaid on each image (with the first three contour levels corresponding to 3 sigma, and increasing thereafter by a factor of two per contour level). For sources detected only in one X-ray band (hard or soft), we show the contours from that band only; these sources are indicated by upper limits in the corresponding X-ray band in Table 4. In all images, North is to the top and East is to the left.

Fig. 4.— (b) As for Fig. 4a.

Fig. 4.— (c) As for Fig. 4a.

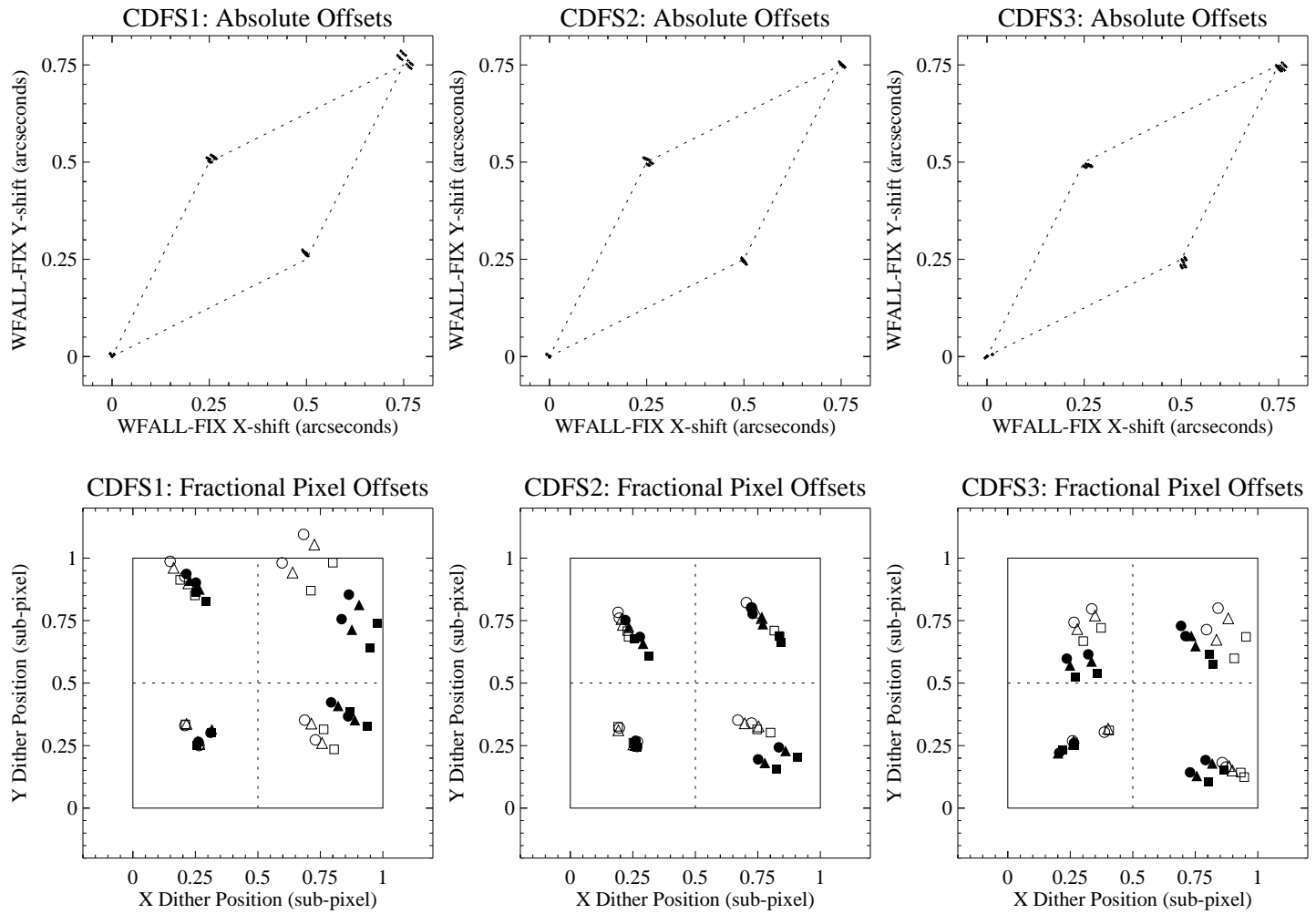
Fig. 4.— (d) As for Fig. 4a.

Fig. 4.— (e) As for Fig. 4a.

Fig. 5.— Color-magnitude diagram of the 3681 sources (small dots) with both F606W and F814W detections in the three WFPC2 fields of this study. Sources with X-ray emission detected in the 1 Msec CDFS image are flagged with larger symbols according to their optical morphology: resolved galaxies of types S0 and earlier (circles); resolved galaxies of types Sa and later (squares); unresolved sources (stars); and indeterminate (triangles). Their size indicates total X-ray flux, while their shading represents X-ray hardness ratio (ranging from white to black for $HR = -1$ to $HR = +1$ respectively). We also show tracks for elliptical, spiral, starburst/irregular and Type 1 AGN template galaxy SEDs as a function of redshift; see text for further details.

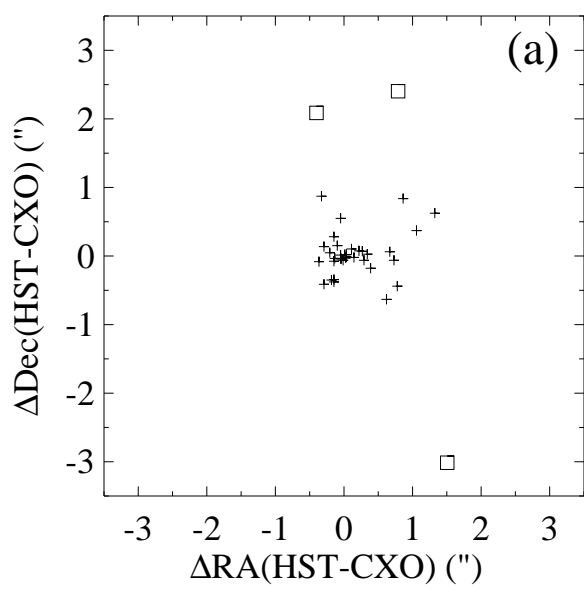
Fig. 6.— *HST* color images of each of the X-ray sources (made by assigning red to F814W, blue to F606W, and green to the average of the two bands). Each image is 8" on a side, with North to the top and East to the left. The objects are generally arranged according to their location on the color-magnitude plot as shown in Figure 5: bright sources near the top, and redder sources toward the right. Some of the source categories are also subdivided according to their hardness ratio. The three non-detections are shown at the bottom.

Fig. 7.— Histogram of the source counts at F814W, in bins of 0.5 magnitude, for the 37 optical counterparts of the X-ray emitting sources, with curves overlaid showing the contribution of various different classes of objects according to the models. Note in particular that the spirals, ellipticals, and Type 1 AGN are all relatively bright, while the Type 2 AGN are the only ones with a distribution that is peaked fainter than $F814W \sim 24$.



This figure "fig3a_cdfs1.jpg" is available in "jpg" format from:

<http://arxiv.org/ps/astro-ph/0110385v1>



This figure "fig3b_cdfs2.jpg" is available in "jpg" format from:

<http://arxiv.org/ps/astro-ph/0110385v1>

This figure "fig3c_cdfs3.jpg" is available in "jpg" format from:

<http://arxiv.org/ps/astro-ph/0110385v1>

This figure "fig4a_subimages.jpg" is available in "jpg" format from:

<http://arxiv.org/ps/astro-ph/0110385v1>

This figure "fig4b_subimages.jpg" is available in "jpg" format from:

<http://arxiv.org/ps/astro-ph/0110385v1>

This figure "fig4c_subimages.jpg" is available in "jpg" format from:

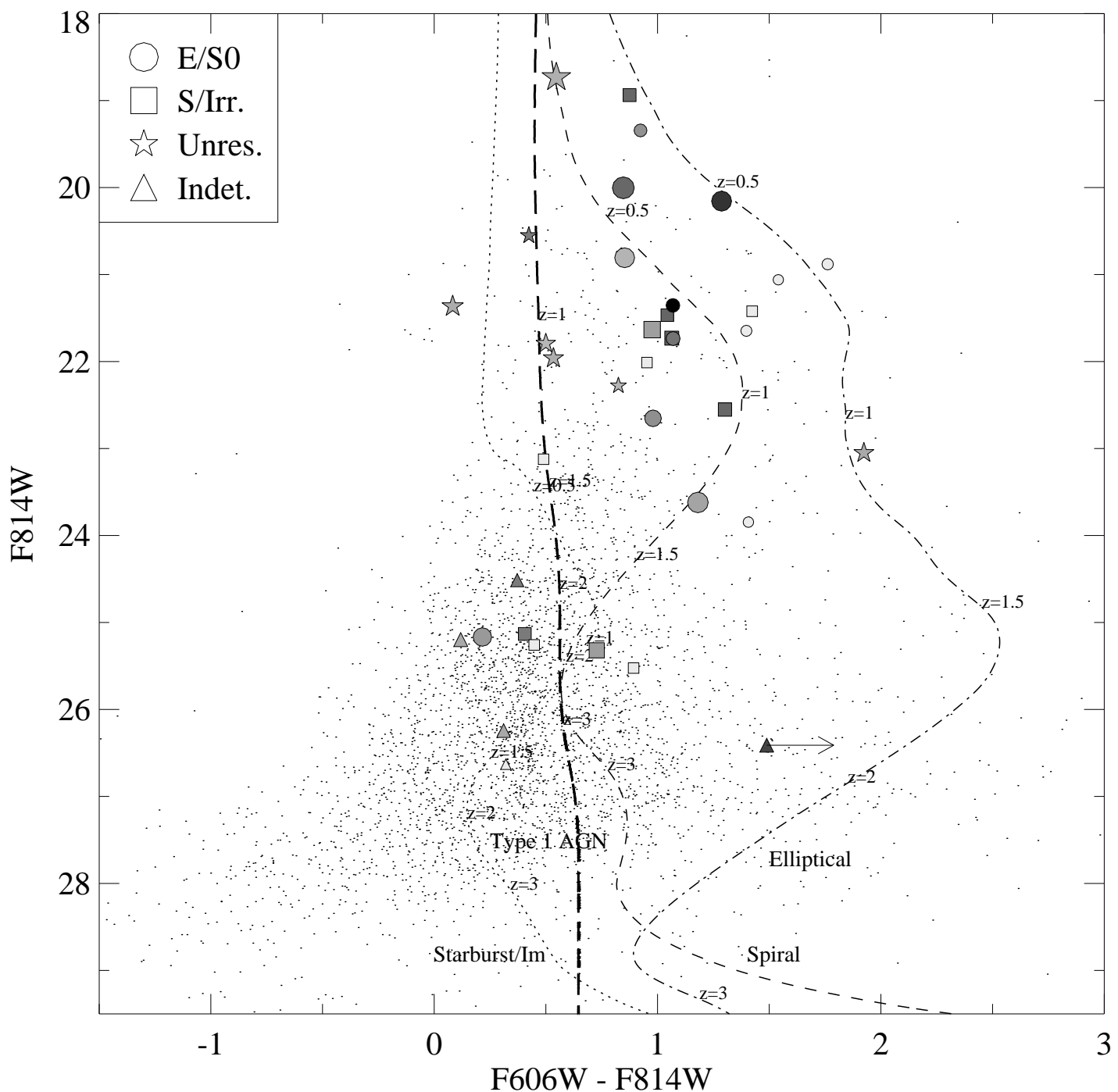
<http://arxiv.org/ps/astro-ph/0110385v1>

This figure "fig4d_subimages.jpg" is available in "jpg" format from:

<http://arxiv.org/ps/astro-ph/0110385v1>

This figure "fig4e_subimages.jpg" is available in "jpg" format from:

<http://arxiv.org/ps/astro-ph/0110385v1>



This figure "fig6_subimages_rgb.jpg" is available in "jpg" format from:

<http://arxiv.org/ps/astro-ph/0110385v1>

